The Interaction of Clouds and Dry Air in the Eastern Tropical Pacific

Paquita Zuidema and Brian Mapes

Rosenstiel School of Marine and Atmospheric Sciences, University of Miami, Miami, Florida

Jialin Lin

NOAA/Earth System Research Laboratory, and CIRES, University of Colorado, Boulder, Colorado

Chris Fairall and Gary Wick

Physical Sciences Divsion, NOAA/Earth System Research Laboratory, Boulder, Colorado

ABSTRACT

Cloud radar observations of eastern Pacific intertropical convergence zone cloud vertical structure are interpreted in light of soundings, 100-km-scale divergence profiles calculated from precipitation radar Doppler velocities, and surface rain gauge data, from a ship at 10°N, 95°W during the 2001 East Pacific Investigation of Climate (EPIC) experiment. The transition from convective to stratiform rain is clear in all four datasets, indicating a coherence from local to 100-km scale. A novel finding is dry air intrusions at altitudes of 6–8 km, often undercutting upper-level ice clouds. Two distinct dry air source regions are identified. One is a relatively dry area overlying the cooler waters of the Costa Rica oceanic thermocline dome, centered approximately 400 km east-northeast of the ship site. The other is the even drier near-equatorial subsidence zone south of 6°–7°N. The former source is somewhat peculiar to this specific ship location, so that the ship sample is not entirely representative of the region.

The 20–25 September period is studied in detail, as it depicts two influences of the dry air on cloud vertical structure. One is the modulation of small-scale surface-based convection, evident as a weakening and narrowing of cloud radar reflectivity features. The other springs from intense sublimation cooling as differential advection brought snowing anvil clouds over the dry layers. During one half-day period of strong sublimation, the cooling rate is inferred to be several tens of degrees per day over a 100-hPa layer, based on a heat budget estimate at 100-km scale involving the horizontal wind divergence data. This is consistent with fluxing ice water contents of 0.05–0.10 g m^{-3} derived from the cloud radar reflectivities. The temperature profile shows the dynamically expected response to this cooling, a positive–negative–positive temperature anomaly pattern centered on the sublimating layer. A buoyancy-sorting diagnostic model of convection indicates that these upper-troposphere temperature anomalies can cause premature detrainment of updrafts into the lower part of the cloudy layer, a feedback that may actively maintain these long-lasting dense anvils.

Middle-troposphere southerly dry air inflow is also evident in large-scale analysis. Given the proximity of the dry equatorial subsidence zone to the eastern tropical Pacific, the differential advection of dry and cloudy air, the ensuing sublimation, and its dynamical aftereffects may play a role in establishing the region's climate, although the extent of their significance needs to be further established.

1. Introduction

Tropical deep convection serves as an engine for the global general circulation through its release of copious latent heat. The set of moist processes in convection modulates further convection, surface and radiative fluxes, and ultimately sea surface temperatures (SSTs). Clouds are the visible expression of these moist processes and strongly redistribute longwave and shortwave radiation. A meaningful understanding of how, when, and where deep convection operates requires a description and interpretation of the convective cloudiness itself.

Corresponding author address: Dr. Paquita Zuidema, Rosenstiel School of Marine and Atmospheric Sciences/MPO, 4600 Rickenbacker Causeway, Miami, FL 33149-1098.
E-mail: pzuidema@miami.edu

One recent source of observational understanding of tropical cloud distributions is data from the Tropical Ocean Global Atmosphere Coupled Ocean–Atmosphere Response Experiment (TOGA COARE; Webster and Lukas 1992). Johnson et al. (1999), relying on precipitation radar and sounding data, documented a trimodal aspect to convective cloud tops for TOGA COARE that included a population of cumulus congestus with cloud-top heights between 4.5 and 9.5 km, as well as trade wind cumulus (~2 km cloud-top height) and deep cumulonimbus (12–16-km cloud-top height). Only the two latter cloud groups are emphasized within early views on tropical clouds (e.g., Riehl 1954). The midtroposphere convective cloud populations have been linked to the presence of stable layers at the melting level (Johnson et al. 1996), extremely dry air aloft (Brown and Zhang 1997; DeMott and Rutledge 1998), and diminished stability between 600 and 800 mb (Yasunaga et al. 2003; Zuidema 1998).

The dry layers inhibit cloud vertical development both through mixing, which increases the density of the entraining parcel (Redelsperger et al. 2002), and through the radiatively induced thermal inversion at the base of the dry layer (Mapes and Zuidema 1996), which reduces the parcel buoyancy relative to its environment. The strong sensitivity of a cloudy parcel to temperature inversions apparently reflects the small background buoyancy of the clouds (Wei et al. 1998). It is also known that dry air layers within the tropical western Pacific troposphere are not a consequence of adiabatic subsidence, and instead correspond to air masses, usually from the extratropical upper troposphere, that often have traveled for a number of days, radiatively cooling along the way (Cau et al. 2005; Mapes and Zuidema 1996; Numaguti et al. 1995; Waugh and Polvani 2000; Yoneyama 2003; Yoneyama and Parsons 1999).

While dry air intrusions over the western tropical Pacific warm pool are by now well studied, their presence within other oceanic tropical convective regions has received less scrutiny. This paper focuses on dry air intrusions observed in the eastern Pacific intertropical convergence zone (ITCZ), during the East Pacific Investigation of Climate (EPIC; Raymond et al. 2004) experiment conducted in September–October 2001. A time–height series of sonde relative humidities taken from the research vessel *Ronald H. Brown*, shown in Fig. 1, reveals several periods with very dry midtroposphere air layers [<40% relative humidity (RH)]: 14 (3–5 km), 19–21 (4 km and higher), 22 (6–7 km), and 29 September (5–8 km). Some but not all were sufficient to noticeably reduce the water vapor content integrated over 2–10 km (Fig. 1, middle).
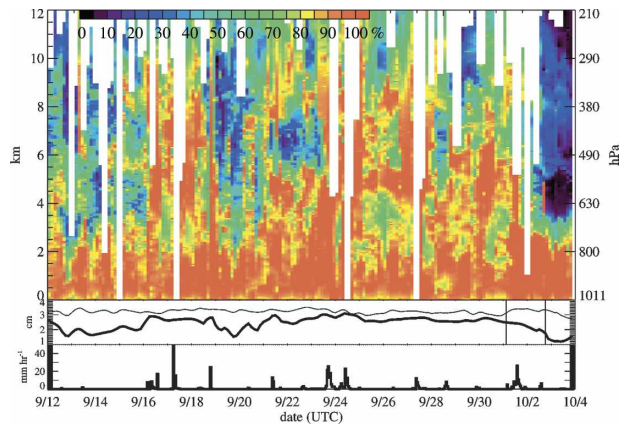

FIG. 1. (top) Relative humidity time series composed from 6 per day rawinsondes. (middle) Integrated water vapor content between 0–2 (light line) and 2–10 km (thick line). Two solid vertical lines indicate when the *Ronald H. Brown* left 10°N (1 Oct), moving southward along 95°W, and when the ship arrived at 5°N (2 Oct); (bottom) 1-hourly surface rainfall rates.

The dry air layers appear abruptly, sometimes within the sonde sampling frequency of 4 h, indicating an advected origin, rather than gradually as would be expected if local radiative subsidence of ~400 m day^{-1} were the source. Even without an examination of the wind fields, Fig. 1 suggests one possible source for the dry air layers: the markedly drier free troposphere apparent after 2 October, when the R/V *Brown* began moving southward into the near-equatorial subsidence region. This constant nearby source of extremely dry air differentiates the eastern Pacific ITCZ from that of the western Pacific.

The objective of this study is to document the origin of the dry layers and investigate how the dry layers interact with convection in the EPIC region. An unusual aspect of the EPIC field campaign was the inclusion of a vertically pointing Doppler cloud radar (not available during TOGA COARE), as well as a scanning Doppler precipitation radar, collocated on the *Brown*. This allows for a more detailed documentation of dry air–cloud interactions within the context of larger-scale divergence features. The next section describes these primary data sources. Section 3 provides experiment-mean cloud radar and rawinsonde results, section 4 discusses the 20–25 September time period, from which section 5 develops quantitative inferences. Section 6 places the shipboard measurements in the context of a longer east Pacific climatology, and section 7 presents a summary.

2. Data

An overview of the EPIC experiment is provided by Raymond et al. (2004). A main purpose was to examine

the processes governing convection within the eastern Pacific ITCZ. The focus of this paper is primarily on the time period that the *Brown* remained stationary in the ITCZ at 10°N and 95°W, from 12 September until 1 October 2001. After 1 October, the *Ronald Brown* moved south along 95°W, reaching 5°N by late in the day on 2 October and 2°N on 3 October.

a. 8.66-mm cloud radar

The vertically pointing K_α-band radar (34.6-GHz frequency; 8.66-mm wavelength) has a beamwidth of 0.5°, and a sensitivity of -46 dBZ at 5 km without attenuation, reducing to -40 and -34 dBZ at 10- and 15-km altitude, respectively (Moran et al. 1998). The original temporal resolution is approximately 9 s for each of four modes, each representing a different tradeoff in sensitivity and range. These four modes are merged into a 1-min resolution composite with a vertical resolution of 45 m. The radar receiver saturates at approximately 20 dBZ.

Surface-based millimeter wave cloud radars are capable of detecting clouds at high altitudes in tropical precipitation-free atmospheres (Comstock et al. 2002), but within convective regimes concern arises about attenuation by precipitation (Lhermitte 1990). Despite this concern, the boundaries of clouds overlying precipitation can still be identified as long as the cloud radar reflectivities are not too attenuated by rain. The strongest precipitation events tend to occur infrequently, so that complete attenuation may also be relatively infrequent. Such statistics have previously been demonstrated for a tropical convective island site (Hollars et al. 2004).

A quantitative estimate of the attenuation is made utilizing surface rainfall rates at the ship as a proxy for the rain rate within an atmospheric layer. The surface rainfall rate frequency distribution at the ship is shown binned linearly within each decade interval, thereby clearly depicting both low and high rainfall rates (Fig. 2). Surface rain rates exceeding 0.01 mm h^{-1} occurred for 20% of the field experiment duration, consistent with the frequency of cloud radar scans possessing downward Doppler velocities greater than 3 m s^{-1}, a separate indicator of precipitation.

The attendant atmospheric attenuation at K_α-band frequencies is shown to relate linearly to rainfall rate within Matrosov (2005) according to his Eq. (3): $a = cR$, where a is the one-way attenuation in dBZ km^{-1}, R is the rain rate in mm h^{-1}, and c is a constant equal to 0.28. For a layer-averaged rain rate of 1 mm h^{-1} between the surface and 5 km, the approximate 0°C level, the total two-way attenuation is 2.8 dBZ. To suffer complete attenuation at a depletion ΔdBZ of 45 dBZ,
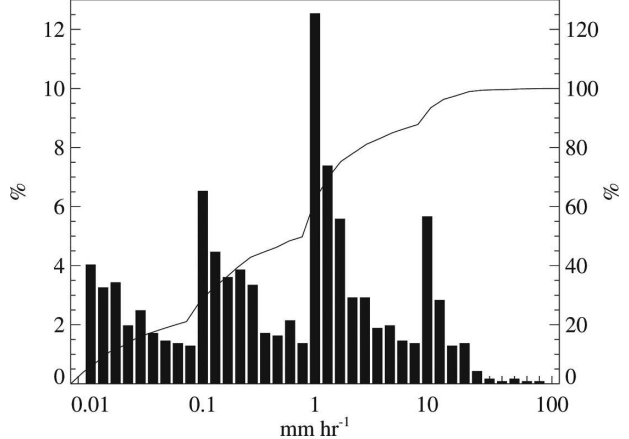

FIG. 2. Frequency distribution of 5-min surface rainfall rates during times when precipitation ≥ 0.01 mm h^{-1}, binned in linear increments between each decadal increase. The sawtooth structure is caused by the 10-fold increase in bin width with each order of magnitude. The cumulative distribution (solid line) is shown as a function of the same precipitation rate binning and corresponds to the right y axis.

rain rates must equal or exceed 16 mm h^{-1}, using $R = \Delta$dB$Z/(2c\Delta z)$ with a Δz of 5 km. Rain rates that large occurred for only 1.5% of the entire field experiment time.

Partial attenuation from rain, arbitrarily thresholded as an attenuation exceeding 3 dBZ, will occur for all rain rates exceeding 1 mm h^{-1}. This occurred almost 10% of the time, a nonnegligible amount. When time series of cloud radar measurements are shown hereafter, surface rainfall rates are included to aid interpretation.

In addition the cloud radar reflectivities are used to estimate ice water contents according to IWC$_K$ = $0.12Z_e^{0.64}$, where $Z_e = 10^{(\mathrm{dB}Z/10)}$ in mm^6 m^{-3} (Matrosov et al. 2003, his appendix A). This $Z - $ IWC$_K$ relationship was developed for single-layer all-ice-phase clouds from diverse, primarily midlatitude, field experiments by comparing radar reflectivities to surface-based infrared radiometer measurements (which are sensitive to cloud optical depths for optical depths <6). We neglect the impact of dry air and water vapor attenuation upon the radar reflectivity values for the ice water content (IWC) estimates.

b. 5.4-cm precipitation radar

The C-band radar operates at a 5.595-GHz frequency and has a 0.95° beamwidth and a 250-m gate spacing. We utilize the results of Mapes and Lin (2005), whereby hourly horizontal wind divergence profiles and their errors are estimated from a velocity–azimuth
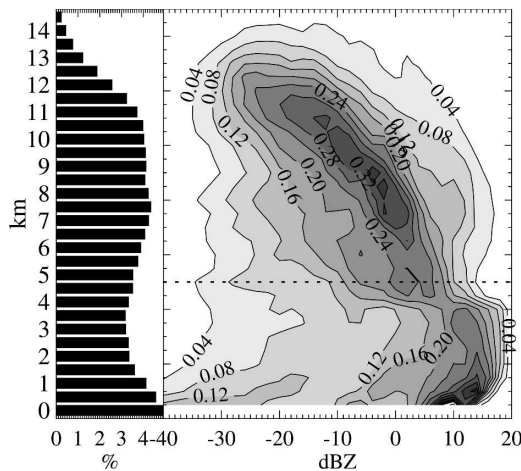
FIG. 3. (left) Normalized frequency by height diagram of all the EPIC radar reflectivities exceeding −45 dBZ. (right) Normalized contoured frequency by altitude diagram, following Yuter and Houze (1995), of EPIC cloud radar reflectivities, binned by 2 dBZ and 500 m. Contour levels are shown in increments of 0.04. The mean 0°C level is indicated by a dotted line.
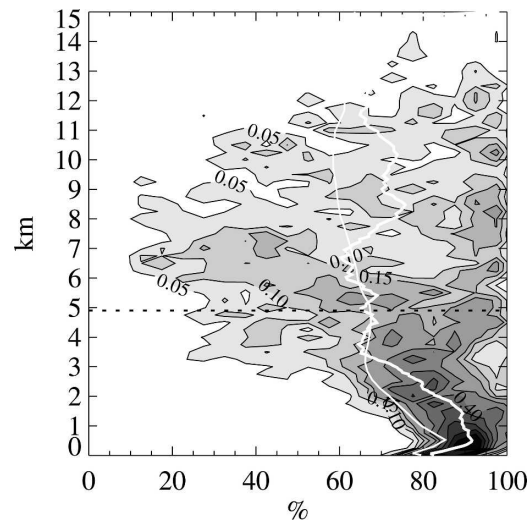

FIG. 4. Normalized frequency distribution of sounding RHs by height, binned by 5% RH and 250 m, with the experiment-mean RH and mean TOGA COARE RH superimposed as thick and thin white lines. RHs at temperatures less than 0°C are with respect to ice. The mean TOGA COARE sounding has been corrected for near-surface dry biases (Ciesielski et al. 2003). The 0°C level is indicated as a black dotted line.

display analysis applied to the mean Doppler radial velocities at different radius ranges (20–60 km). The radial velocities are initially dealiased and corrected for hydrometeor fall using a simple fall speed assumption. Mapes and Lin (2005) found the EPIC data to be of exceptional quality and coverage, allowing creation of a regular time series encompassing the length of the field experiment. The time series thereby includes weather conditions subtler than the rain events for which velocity–azimuth display analysis has traditionally been applied.

c. Soundings and surface rainfall rates

Six Vaisala RS80 sondes were released per day, at approximately 0300, 0700, 1100, 1500, 1900, and 2300 UTC, for a total of 106 released at 10°N, 95°W, from 12 September until 1 October. The extent of their vertical ascent is evident in Fig. 1. Occasionally they were observed to fail in the middle troposphere during rain events, apparently from the weight of wet snow on the balloons. Reported surface rainfall rates are a melding of quality controlled rates recorded by shipboard optical rain gauges (F. Bradley 2004, personal communication).

3. Experiment-mean distributions

a. Cloud radar

A frequency distribution of the entire cloud radar reflectivity dataset by height and radar reflectivity is shown in Fig. 3. Two distinct low-altitude cloud populations are evident. One extends up to ~1.5 km with

low (≤−15 dBZ) radar reflectivities, representative of trade wind cumulus. The other possesses radar reflectivities approaching the saturation value of 20 dBZ at the lowest levels and attenuating upward, corresponding to precipitation. The mean 0°C level is indicated at 4.9 km, although it tends to be depressed by a few hundred meters during precipitation. At the 0°C level, the most frequently occurring reflectivity mode shifts abruptly from ~12 to ~7 dBZ, as the predominant phase shifts from liquid to ice and the complex dielectric constant decreases accordingly. A decrease with height of the most frequently occurring reflectivity is evident above the 0°C level, as the radar attenuates and moisture contents decline with altitude. The decrease is smooth, but has a peak along the "mode" ridge at ~−5 dBZ between 8 and 9 km defined by smaller values between 5 and 7 km. Total detected cloud decreases above 11 km, with little cloud detected above 14 km. A slightly enhanced population of low radar reflectivities is evident at the mean 0°C level of 4.9 km, perhaps altocumulus clouds detrained at the freezing-level stable layer (Johnson et al. 1996). Populations of clouds with low radar reflectivities are also apparent from 7 to 8 km and above 10 km.

b. Rawinsondes

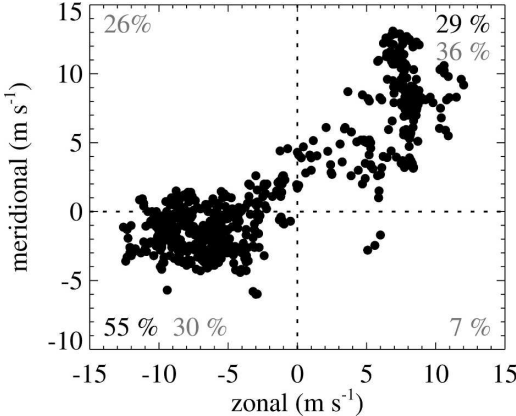The probability distribution of RH by height and the mean RH profile are shown in Fig. 4. From the surface

FIG. 5. Rawinsonde meridional vs zonal winds, for 50-m thick air layers between 4 and 8 km with RHs ≤30%. Lower-left and upper-right regions indicate winds from the east-northeast and southwest, respectively, with the percentage of observations relative to the total indicated in black. Percentages for all layers regardless of RH value are indicated in gray.

FIG. 6. Rawinsonde meridional winds (color scale at top of figure).

up to almost 3 km the atmosphere was consistently moist (RH > 60%) and at 3 km and above the relative humidity distribution bifurcates. One population remains moist while another population of much lower RH values appears. A relative maximum in the frequency of dry air layers occurs between 6 and 8 km. The mean relative humidity profile from the TOGA COARE Intensive Flux Array, based on 2518 corrected sondes collected over a 4-month period, is shown for comparison (Ciesielski et al. 2003). Compared to the TOGA COARE mean profile, the mean RH profile at the ship site is more moist up to 3 km and again above 8 km.

The wind direction when RH <30% within the 4–8-km layer is shown by dots in Fig. 5. The distribution of dry layer winds was distinctly bimodal, with southwesterly winds occurring 29% of the time, and east-northeasterly winds 55% of the time. For comparison, the unconditional percentages of time when wind direction was from each quadrant, regardless of RH, are indicated in gray. The passage of three easterly waves during the EPIC experiment (Petersen et al. 2003) is evident in unfiltered meridional winds,[1] shown in Fig. 6. Although southwesterly middle-troposphere winds can be either moist or dry, a correspondence is evident between the strongest southerly winds (red areas in Fig. 6) and the dry layers shown in Fig. 1.
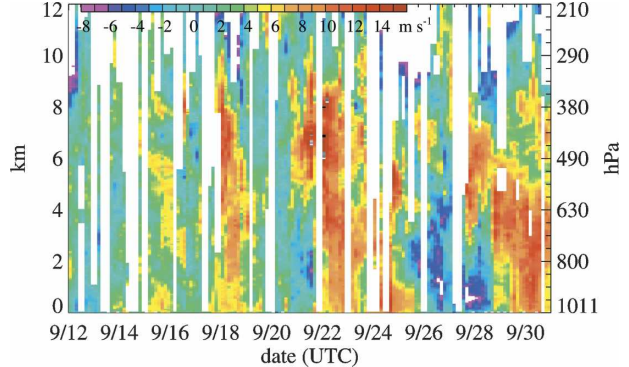
---

[1] The southerly and northerly easterly-wave phases are identified as 700-mb meridional winds exceeding +2 and −2 m s^{-1}, respectively, with the ridge and trough phase corresponding to the transition from a southerly to a northerly wind regime and vice versa.

4. 20–24 September time series

An especially interesting period is shown in Fig. 7, where cloud radar reflectivity structure is overlaid by 6-times-daily wind and RH profiles and divergence contours. A lower panel for each day depicts surface rainfall. These 5 days included an east-northeasterly dry air intrusion (20 September) and a longer-lived southerly dry air event (21–23 September). Occasional showers become more frequent, then finally are followed by two major multihour rain events on 23–24 September (note logarithmic rain-rate scale). These rain events occurred in the far field of Hurricane Juliette (visible image in Fig. 9).

On 20 September (Fig. 7a), winds were primarily from the east-northeast throughout the depth of the free troposphere. Dry air layers at varying heights and thicknesses can be seen, and the sounding-integrated water vapor contents were low (Fig. 1). Fractional cloud cover was low. Some convection and light rain occurred over the ship, but nothing extensive or deep. The coincidence of cloud-top height with dry air at about 8 km may indicate that this air discouraged convection, as was independently observed in aircraft dropsonde data (Raymond et al. 2003, their Fig. 15). The wind divergences for this day are not shown, as they were small and did not correspond well to the overhead cloud features.

In contrast, the weather on 21–24 September (Figs. 7b–e) was highly complex, with greater, longer-lasting surface rainfall rates and more dramatic cloud and divergence features. Tropical Storm Juliette developed to the north of the ship on 21 September (Fig. 8). It moved slowly northwestward thereafter, and was upgraded to a hurricane on 23 September (Fig. 9). Beyond Juliette's outer bands, separate mesoscale convective systems (MCSs) developed southeast of the ship, possibly associated with a warm sea surface temperature anomaly
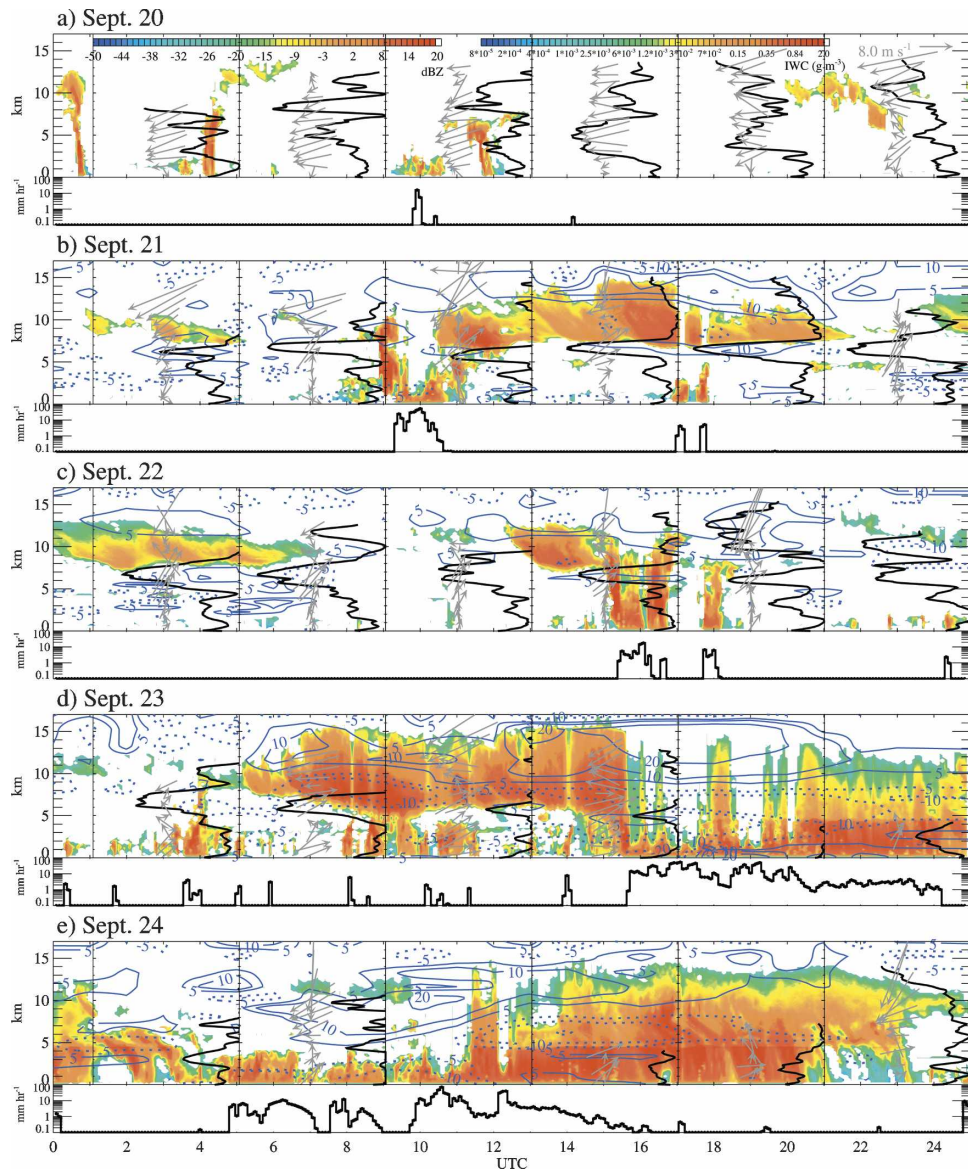
FIG. 7. Cloud radar reflectivities (color) for (a)–(e) 20–24 Sep, overlaid with the sounding RHs (black curves within a 0%–100% range delineated by vertical axis lines), winds (gray vectors), and hourly wind divergence averaged over a 44-km radius circle around the ship (contours, units 10^{-5} s^{-1}, omitted for 20 Sep). Winds and RH profiles are centered on the sonde launch times (approximately 0300, 0700, 1100, 1500, 1900, and 2300 UTC). Surface rainfall rates are plotted below each panel. One hour from the subsequent day is shown at the end of each day for clarity. An estimation of the IWCs can be made using the right-hand key in (a).

(Wijesekera et al. 2005). The MCS shown in Fig. 9 moved westward, passing over the ship on 23 September. Another MCS (re)developed to the west of the ship on 24 September, based on inferences made from satellite infrared imagery.

A 2-km-thick dry air layer centered at approximately 7 km advected in from the south-southwest beginning on 21 September and continuing until 23 September.

Erosion of surface-based convective cloud towers by this dry layer is occasionally apparent as a reduction in the cloud radar reflectivities (Fig. 7b, 21 September, 0900 UTC; Fig. 7c, 22 September, 1800 UTC). Above 8 km, the winds were northeasterly and intermittently advected in cirrus clouds, sometimes quite thick ones. These upper-level clouds tended to be associated with convergence near cloud base and divergence near cloud
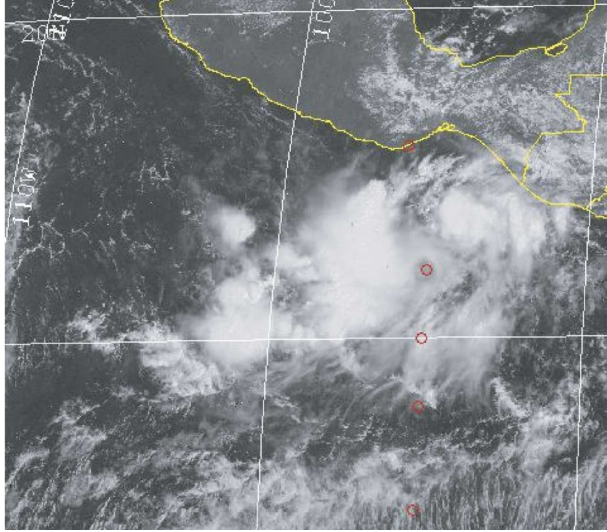
FIG. 8. The 1645 UTC 21 Sep *GOES-8* visible image. The 10°N latitude and the 100° and 110°W longitudes are indicated (white lines), and the ship site is indicated by the red circle along the 10°N line (other red circles indicate buoys).

FIG. 9. Same as in Fig. 8, but for 1645 UTC 23 Sep.

top (e.g., 21 September, 1600–2200 UTC; 22 September, 1400 UTC), indicating anomalous rising motion in the cloud layer. This association also indicates that the overhead cloud was representative of impacts over a surrounding region of at least 50-km radius. Also notable is the divergence sometimes present in the dry air layer beneath cloud base (21 September, 0200–0400 UTC and 1000–2000 UTC).

On 23 and 24 September (Figs. 7d,e), convection at the ship site was much more intense, with two major mesoscale rain events of several hours duration. Consistency is apparent among the two radar datasets, surface rainfall rates, and soundings, and thus between local and ~100-km scales. The case of 24 September (Fig. 8e) shows the classic progression of convective and stratiform rainfall especially clearly. Initially (0500–1000 UTC), convergence below 3 km and divergence above in the 5–10-km layer coincided with showery rains and relatively shallow radar echoes. From 1000 to 1300 UTC, the divergence layer rose as convection deepened, the balloon sounding failed, and heavily attenuated cloud radar reflectivities were observed along with heavy surface rain. After 1300 UTC the midlevel convergence characteristic of stratiform precipitation developed, associated with a mesoscale updraft in the upper troposphere and downdraft in the lower troposphere. Unsaturated conditions are seen in the lower troposphere (where high relative humidities were almost never observed; Fig. 4). The 1500 UTC sounding terminated at the 0°C level, typical of stratiform rain soundings, owing to the weight of wet snow.

Eventually the surface rain ceased while the radar showed fallstreaks (virga) in the lower troposphere for several more hours.

5. 21 September ice sublimation and its thermodynamic impact

Anvil sublimation has been studied extensively in connection with midlatitude squall lines, where it is thought to contribute to descending rear-inflow jets observed along the underside of trailing stratiform anvil clouds (Smull and Houze Jr. 1987; Stensrud et al. 1991) and is associated with large cooling rates (Gallus and Johnson 1991). Anvil sublimation in the Tropics appears to have received less attention. On 21 September, the development of Juliette to the north sustained a thick snowing anvil cloud over the boat. This was undercut by a pronounced dry layer (Fig. 7b), resulting in ice sublimation that we investigate in more detail here for the 1400–2100 UTC time period. A cooling rate is first derived using the ~100-km scale wind divergence data, based on dynamical considerations. This cooling rate is then converted to an estimate of ice water content for comparison to retrievals based on the cloud radar data.

a. Sublimation rate and ice water content

The cooling rate implied by the precipitation radar's wind divergence data can be estimated from an analysis of leading terms in the heat budget. For local intense diabatic events in the tropical troposphere, the leading-order balance is $Q \sim \omega\sigma$, where Q is heating rate (ex-
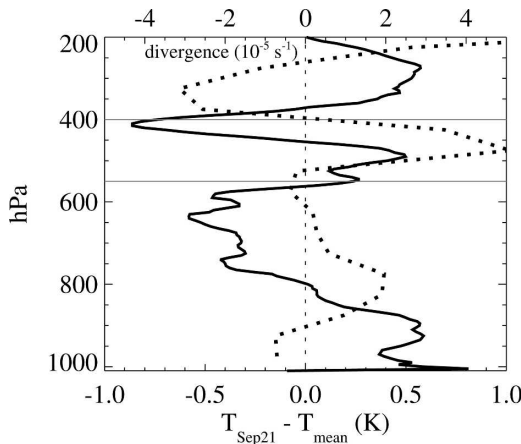
FIG. 10. Temperature difference between the 1400, 1800, and 2200 UTC 21 Sep mean sounding and the 106-mean sounding, with the approximate dry layer boundaries indicated (gray lines), and the mean 1300–2000 UTC divergence profile (dotted line; units of 10^{-5} s^{-1}).

pressed as a temperature tendency in K per day), σ is a static stability parameter, and ω is vertical velocity in pressure coordinates. Temperature changes and horizontal advection are neglected, as they are usually secondary, and indeed are typically smaller than the errors incurred in estimating ω. In the ship-mean σ profile, a nearly constant value of -6 K per 100 hPa prevails in the 400–500-hPa (5.8–7.6 km) layer. This allows the vertical gradient of Q to be simplified as $\delta Q/\delta p \sim \delta\omega/\delta p = \sigma D$ by mass continuity, where D is horizontal wind divergence. We apply this equation to the $\sim$100-hPa sublimation zone in the upper portion of the dry layer. At the bottom of the sublimation zone, $Q \sim 0$, since radiation is the only diabatic process and the dryness and overcast sky minimize radiative cooling. The cooling rate Q at the top of the sublimation zone is then given by $\Delta Q \sim \sigma D \Delta p$, which is readily evaluated for $\Delta p = 100$ hPa and $D \sim 5 \times 10^{-5}$ s^{-1} (the time-mean, layer-mean divergence over a 44-km range) to yield $Q \sim -30$ K day^{-1}.

In the face of such strong cooling, we must revisit the assumptions that temperature and σ are constant, with climatological values. In fact, the temperature profile had a fairly strong anomaly during this period, as shown in Fig. 10, where a heavy solid curve shows the difference between the temperature of the last three soundings from 21 September and the mean of all 106 soundings. The dry layer is indicated from 400–550 hPa, and a sublimation-induced cold anomaly of almost 1 K is seen at its upper edge. The cold anomaly is sandwiched between warm anomalies. As shown in Mapes and Houze (1995, their Fig. 20) for the more common case of intense cooling from the melting of snow at the 0°C

level, the warm anomalies represent the linear response of the stratified atmosphere to localized diabatic cooling, with Fig. 10 reflecting the residue after the longer vertical wavelengths have been dispersed by gravity waves.

Our estimate of Q can be refined by reference to Fig. 10. The 21 September temperature structure reduces the magnitude of σ by about 25%, to -4.5 K per 100 hPa, thereby reducing the cooling rate estimate to ~-22 K day^{-1}. This value neglects horizontal advection and assumes steady-state conditions, terms we suspect are negative—fostering stronger cooling—but small. Although the 21 September temperature profile also implies a vertical gradient in σ, and therefore a $\omega\delta\sigma/\delta p$, we believe this term is small, noisy, and negligible. In sum we estimate a slightly stronger time-mean Q at $\sim-25 \pm 5$ K day^{-1}, with the uncertainty based on variations of the independent D estimates from different-sized circles (28-, 44-, and 60-km radii), which we think to be the dominant source of uncertainty.

Equating this dynamically derived estimate of Q to the latent cooling by phase change in a steady, horizontally homogeneous shower of particles evaporating over a depth δz gives

$$Q \approx \frac{L_s}{\rho_a c_p} \frac{\delta(\text{iceflux})}{\delta z} = \frac{L_s}{\rho_a c_p} \frac{\delta(\text{IWC})(V_z)}{\delta z}, \quad (1)$$

where ρ_a is the air density, c_p is air's heat capacity at constant pressure, L_s is the latent heat of vaporization of ice, IWC is ice water content, V_z is mean particle fall speed, and z is altitude. We can evaluate this equation to yield an estimate of IWC, labeled as IWC_{dyn}. The mean cloud radar Doppler velocity over the 500–400-hPa layer was -1.3 m s^{-1}. We neglect the mean air vertical motion (estimated from the divergence as an order of magnitude smaller) and dry air density changes, and take this value to represent a typical V_z. An evaluation of Eq. (1) yields an IWC_{dyn} of about 0.08 g m^{-3}.

It is instructive to compare this value to a direct retrieval of IWC from the K-band reflectivity. We presume the cloudy 500 m of each radar scan located nearest the dry layer top to be sublimating (excluding the lowest such radar gate). We find a layer-mean, time-mean value for IWC_K of 0.08 g m^{-3}. This approximately agrees with the IWC_{dyn} estimated from the wind divergence, with a coincidentally remarkable correspondence reported here. Cloud radar ice water content retrievals are difficult to validate for high, optically thick clouds. The bulk-averaged results are crude, but they provide an independent comparison to satellite-based retrievals of a comparable spatial scale and are
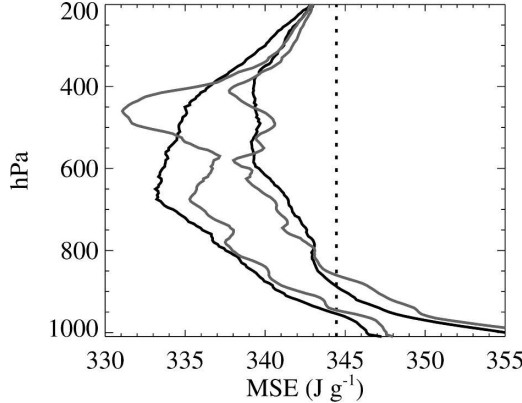
FIG. 11. MSE and saturated MSE calculated from the mean sounding (black lines) and from the mean of 21 Sep, 1400, 1800, and 2200 UTC soundings (gray lines). The dotted line indicates the MSE of a surface parcel of 100-hPa thickness.
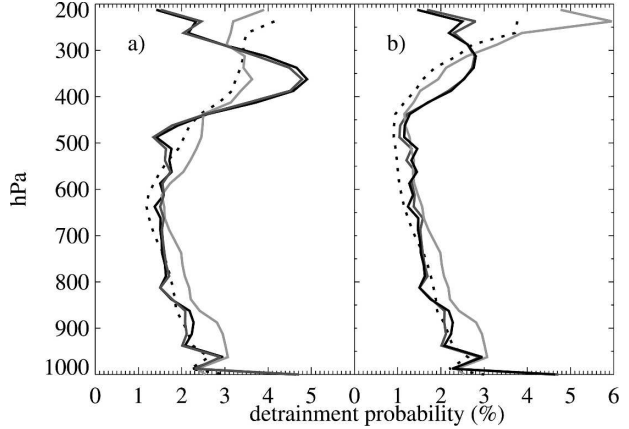

FIG. 12. Mean vertical profiles of detrainment probability from the Raymond–Blyth buoyancy-sorting cloud model computed from all soundings (black dotted line), from the 1400, 1800, and 2200 UTC 21 Sep rawinsondes (black line), and from the 1400, 1800, and 2200 UTC 21 Sep rawinsondes with the mean moisture structure substituted for the actual RHs (dark gray line, almost overlaid on the black line) and with the mean temperature structure substituted for the actual temperatures (light gray line): (a) not including ice effects and (b) including ice effects. A liquid water loading of 3 g kg^{-1} is assumed. Inflow layers, of 5-hPa thickness, are only evaluated up to 110-hPa altitude.

not strongly limited by the multilayering of clouds. The results also imply a representativeness that nicely complements more jittery in situ validations.

b. Feedback to convective detrainment via buoyancy

The thermal structure seen in Fig. 10 is large enough to have a major effect on the detrainment profile of deep convection in the vicinity. Both moisture and temperature anomalies in the 21 September three-sounding composite sounding can be seen in the profiles of moist static energy (MSE) and saturation MSE (MSE$_{sat}$), shown in Fig. 11. Black curves show the 106-sounding mean, while gray shows the 21 September composite. The dry layer mean mixing ratio was approximately 1 g kg^{-1} compared to a value of approximately 2.5 g kg^{-1} for the 106-sounding average, a difference which could be significant when mixed with air rising from low levels with a mixing ratio of 17 g kg^{-1}. However, arguably more important to the buoyancy of convective parcels at higher altitudes is the ambient temperature anomaly.

Rather than rely on traditional graphical consideration of such MSE diagrams, the impacts of moisture and temperature variations upon parcel buoyancy were investigated with the Raymond–Blyth buoyancy-sorting model (Raymond and Blyth 1992). The model envisions near-surface air parcels ascending to all levels below their highest level of undiluted neutral buoyancy, and at each level undergoing mixing with environmental air. These mixtures, assumed to have a uniform distribution of mixing fractions (in practice nine mixtures with fractions 0.1–0.9) then sort themselves out by detraining at the level where they achieve neutral buoyancy. The statistics of these detraining mixtures define

a "probability" of detainment plotted in Fig. 12. Results are shown of outflow probability derived from such computations on all 106 soundings, from the three 21 September soundings alone, and from two modified versions of the 21 September soundings. Uncertainties about ice processes are bracketed by the two panels, with no freezing at left and complete thermodynamic equilibrium at right.

The 106-sounding results show detrainment increasing with height up to and beyond the highest level indicated (250 hPa, 12 km). The 21 September profiles show more parcels detraining instead at lower altitudes, with the enhancement peaking near the 350-hPa level. To isolate the effects of dryness, the 106-sounding-mean humidity structure was substituted for the actual moisture structure, with the temperature structure unaltered. Results are almost unchanged (dark gray curves almost on top of black curves). To isolate the effect of temperature, the 106-sounding-mean temperature structure is substituted for the actual temperature in the three soundings from 21 September (light gray line, closer to the long-term mean shown in the dotted curve). Temperature effects are clearly dominant, causing convective updraft mixtures to detrain at the stable layer atop the cold anomaly—that is, right in the lower anvil cloud where a source of condensed ice for the intense sublimation cooling is needed. As is evident in Fig. 11, the ~350 hPa level is where both the MSE and

MSE_{sat} profiles begin to increase rapidly with height, even in the mean, capping the potential instability of parcels in the troposphere and making this area an especially sensitive one for temperature anomalies.[2]

This calculation points to a positive feedback, with sublimation cooling driving dynamical motions that enhance stability above the sublimating layer, leading to detrainment just above the top of the dry layer—fostering more sublimation below. This feedback may help explain the longevity of the situation on 21 September, when 1 m s^{-1} fall speeds like those observed would sediment away 3.6-km-thick anvils in 1 h if the anvils were not being refreshed somehow. Horizontal advection was refreshing the column over the ship, but the original source was surely deep convective detrainment. Such a feedback for the melting level is discussed in Mapes and Houze (1995) and further explored in Mapes (1997) using the Raymond–Blyth buoyancy sorting computation coupled to a dynamical model.

It should also be noted that since the temperature anomalies of 21 September are localized and transient, the air detrained at anvil base will ultimately want to continue rising to its "background" level of neutral buoyancy, perhaps indicated by the 106-sounding mean. This potential for further rising may enhance the potential of detrained air at anvil base for precipitation. Indeed, the strong divergence at anvil top (Fig. 7b) suggests clouds containing vigorous updrafts. Additionally, the sublimation-induced divergence will vertically shrink the sublimating layer and spread it horizontally, although the measurements lack sufficient horizontal context with which to search for this effect. An investigation of these mechanisms with a full-physics numerical cloud model will more clearly establish their significance.

6. Climatological considerations regarding dry intrusions

Backward trajectories along with spatial maps of satellite-derived water vapor paths can further illuminate the origin regions for dry air layers, if vertically integrated water vapor contents are a useful proxy of upper-tropospheric moisture. Backtrajectories were calculated with the Hybrid Single-Particle Lagrangian Integrated Trajectory (HYSPLIT) model assuming motion along an isobaric surface and utilizing National

---

[2] The apparent enhanced detrainment at the 21 September 400-hPa cold temperature anomaly evident in Figs. 10 and 12 reflects averaging and smoothing, with no such effect seen in the individual profiles.
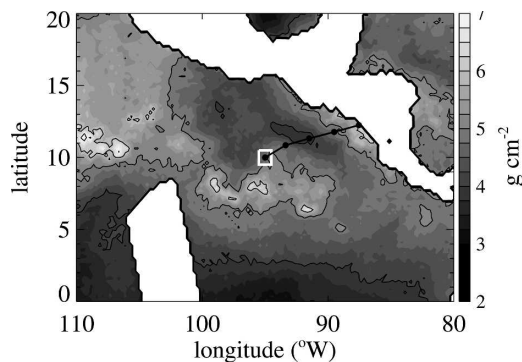

FIG. 13. Water vapor path, retrieved from Special Sensor Microwave Imagery (SSM/I) data collected between 0000 and 1200 UTC on 20 Sep 2001, using Schluessel and Emery (1990). Contour lines are shown every 1 g cm^{-2} and the ship site is denoted by a small white square. A HYSPLIT model backtrajectory from 8 km above the ship site, ending at 0000 UTC, is indicated (black solid line) with filled circles every 6 h. Spatial resolution is 0.25°.

Centers for Environmental Precipitation (NCEP) version 1 analyses. The dry air on 20 September was associated with an east-northeasterly wind, coinciding with the northerly phase of an easterly wave. The backtrajectories trace the air back to a drier area east-northeast of the ship 12 h previous (Fig. 13). The dates 21 and 22–23 September coincided with the trough and southerly phases of an easterly wave, respectively. HYSPLIT air parcel backtrajectories depict an advection of air layers from the south in these cases. Figure 14 shows an example for 22 September, with a water vapor field from 1200 to 2400 UTC and a backtrajectory ending at the ship site at 7-km altitude at 23 UTC. The backtrajectory indicates an origin from an especially dry and northward-protruding part of the equatorial subsidence zone. Interestingly, the backtrajectory implies a mean advection speed of 4.4 m s^{-1} for the previous 6 and 24 h.
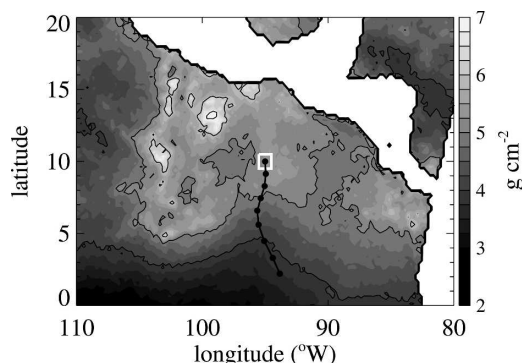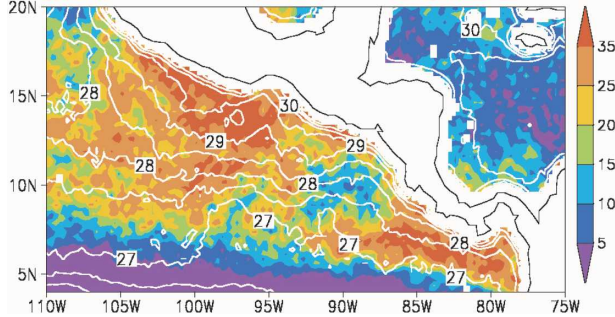

FIG. 14. Similar to Fig. 13 but for SSM/I data collected between 1200–2400 UTC on 22 Sep 2001, with a HYSPLIT model backtrajectory ending at the ship site at 2300 UTC, 7 km altitude.

FIG. 15. 1998–2003 September climatology of TRMM Microwave Imager precipitation (color; mm day^{-1}) and SST (contours; °C). Reproduced from Fig. 9c of Xie et al. (2005).

FIG. 16. NCEP 1990–2000 September mean RH along 95°W from 10°S to 15°N, with mean meridional winds (m s^{-1}) superimposed.

This is significantly less than the rawinsonde wind speed of 15 m s^{-1} and suggests that the NCEP analysis is underestimating the middle-troposphere winds.

These two histories illustrate the two main pathways affecting the EPIC ship location, but it is useful to consider whether they are typical of the region in other years. A 6-yr climatology of the precipitation and SST, derived from the Tropical Rainfall Measuring Mission (TRMM) Microwave Imager according to Wentz et al. (2000) for the eastern tropical Pacific, is shown in Fig. 15, reproduced from Fig. 9c of Xie et al. (2005), and sheds light on the observations shown in Figs. 13 and 14. We will assume that low-precipitation regions are correlated with dry upper atmospheres in the following discussion (e.g., Bretherton et al. 2004).

To the south of the ship lies the well-studied cool oceanic equatorial upwelling zone (e.g., Peixoto and Oort 1992), with the overlying atmosphere providing a ready origin for the southerly dry air intrusions at the ship site. The dryness of the intrusions during September 2001 may have been enhanced relative to a long-term mean. In September, 2001, SSTs were about average at the ship site but were cooler than climatology by approximately 1 degree at 6°–7°N (McGauley et al. 2004, their Fig. 1). This cooler SST to the south may have enhanced free-troposphere dry air inflows, unless stable conditions decoupled its influence.

An interesting feature in Fig. 15 is the low-precipitation slot to the southwest of the ship, which is consistent with the dry layer wind directions observed at the ship (Fig. 5). In September 2001, the SST anomaly pattern along 6°N featured a wavelength of approximately 1000 km and a period of approximately 1 month (McGauley et al. 2004, their Fig. 1b), resembling a tropical instability wave (TIW; Hashizume et al. 2001). The slot in Fig. 15 is coincident with the northward protrusion of the TIW-like SST feature. This slot and associated SST pattern are also apparent in longer-
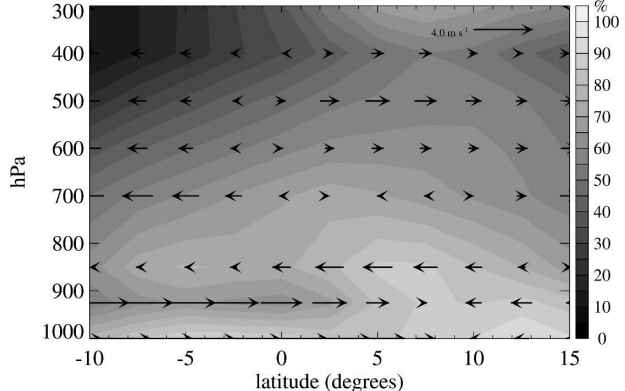
term, better-sampled climatologies (McGauley et al. 2004, their Fig. 1a), suggesting that a more detailed investigation might be worthwhile. One hypothesis is that the land boundary provided by the Central American land chain establishes a preferred TIW-type of SST variation that fosters such a low-precipitation slot.

To the east of the ship site lies the mean shoaling of the oceanic thermocline called the Costa Rica Dome (Xie et al. 2005). Here, wind stresses induce upwelling and ocean mixing, which decreases the sea surface temperature, reducing local precipitation by one-half (Xie et al. 2005). This localized feature of hydrography stems from winds blowing through gaps in the mountain chain along Central America. The precipitation reduction is a more subtle feature than the equatorial subsidence zone; it is also captured by a better-sampled infrared climatology (Xie et al. 2005, their Fig. 10b), but not by the popular Merged Analysis of Precipitation (CMAP; Xie and Arkin 1996) product. The frequent easterly dry air intrusions in EPIC appear to reflect the ship's proximity to the Costa Rica Dome within a prevailing easterly zonal flow. Consistent with this view, the September-mean rainfall east of the ship was less than to the west, according to the C-band radar data.

Reanalysis data from NCEP (Kalnay et al. 1996) suggest that free-tropospheric dry air advection from the south and east is climatological. Easterly dry air advection along 10°N is localized to 95°W, while southerly midlevel flow into the ITCZ is seen more broadly. A 10-yr September mean plot of relative humidity and meridional wind along 95°W shows a midtropospheric (500 hPa) southerly dry flow from the equator to 10°N (Fig. 16), in agreement with the few soundings available in the region (Zhang et al. 2004, their Fig. 2). Observations from the Line Islands Experiment, held farther west at approximately 160°W (Madden and Zipser

1970), and the Global Atmospheric Research Atlantic Tropical Experiment (GATE) also documented an inflow layer below the dominant deep convective outflow layer. On a larger scale, a middle troposphere inflow to convecting regions is seen in the zonal mean cross-equatorial flow from winter to summer hemisphere (Mapes 2001, their Fig. 4), in idealized simulations of the eastern tropical Pacific (Nolan et al. 2006, manuscript submitted to *J. Atmos. Sci.*), and even in idealized cloud-resolving models of large-scale circulations (Grabowski et al. 2000). Fundamentally, this feature springs from the properties of a moist adiabatic temperature profile, which the tropical tropospheric stratification resembles (Mapes 2001).

7. Summary

Eastern Pacific ITCZ cloud vertical structure at 10°N, 95°W has been documented with a vertically pointing cloud radar and interpreted using soundings, 100-km-scale wind divergence profiles calculated from precipitation radar data, and surface rainfall rates. A highlighted finding is of dry air intrusions located at 6–8-km altitude occurring within otherwise moist, convective conditions. Winds associated with the dry air intrusions (Fig. 5) were most frequently east-northeasterly (55% of the data sample), from the cooler water of the Costa Rica Dome, and second, south-southwesterly (29%) from the dry equatorial zone. The most pronounced dry layers corresponded to the strongest southerly winds (Figs. 1 and 6). The longest-lived EPIC event lasted for about 2.5 days, about a half period of the easterly waves characterizing the synoptic weather changes. A 5-day time series (Fig. 7) shows many of the relevant processes during an easterly dry air intrusion (20 September), a southerly dry air intrusion (21–23 September), and two substantial mesoscale convective systems (23–24 September).

Dry air has at least two major impacts on cloud processes. It appears to erode and perhaps suppress small-scale surface-based convective clouds (e.g., 21 September, 0900 and 1700 UTC; 22 September, 1500–1800 UTC), evident as a weakening and narrowing of cloud radar reflectivity features (see also Raymond et al. 2003, their Fig. 15). Dry air also induces intense ice sublimation cooling when advected under thick snowing anvil clouds. In the case of 21 September specifically, a cooling rate of -25 K day^{-1} is computed, corresponding to 0.08 g m^{-3} of ice falling into the top of the dry layer at a speed of about 1.3 m s^{-1}. This is comparable to a more direct retrieval of IWC from cloud radar, providing a unique if crude validation tool.

The sublimation cooling induced a thin layer of cold temperatures locally sandwiched between warm anomalies, similar to the temperature structure generated by melting (Mapes and Houze 1995). The temperature anomalies rather than humidity variations appear to govern the impact of the middle to upper troposphere upon the buoyancy of a convective parcel, according to experiments with a buoyancy-sorting convection model (Raymond and Blyth 1992). These temperature anomalies can enhance deep convective detrainment just above the dry layer (Fig. 12), which may in turn reinforce the snowing anvil clouds, providing a positive feedback.

The possible effects of these upper-level southerly dry air intrusions on surface rain rates are not easily assessed. Dry intrusions preferentially occurred during the wetter southerly phase of the easterly wave cycle (e.g., 21–23 September), with a relatively moister, warmer lower troposphere (Figs. 10 and 11). The main importance of dry intrusions may be as an influence on upper-level clouds. For example, dry intrusions causing lower detrainment levels may contribute to relatively lower cloud-top heights in the eastern Pacific, which are known to produce a low bias in naively applied infrared-based satellite precipitation estimates calibrated for other regions. On the other hand, the subsequent relaxation of the temperature anomalies could foster a more vigorous uprising of the detrained air, thereby enhancing precipitation.

Southerly dry air inflow at 7 km appears to be a climatological feature during September (Fig. 16), at least as far west as 115°W (not shown), with the NCEP analysis possibly underestimating the process. Easterly dry air advection is more localized, with an enhancement at 95°W due to its proximity to the cool water of the Costa Rica Dome in the oceanic thermocline. Inflow to deep convection near 7 km has been observed in other experiments, in larger-scale flows, and in idealized models, for reasons that apparently can be traced back to fundamental thermodynamic properties of water. This suggests that dry layers advecting under moist layers, and the attendant sublimation, will tend to occur wherever very dry air is adjacent to convection. This condition characterizes the eastern Pacific ITCZ and therefore the differential advection contributes to the region's climate, although the extent of the significance requires further investigation.

REFERENCES

Bretherton, C. S., M. E. Peters, and L. E. Back, 2004: Relationships between water vapor path and precipitation over the tropical oceans. *J. Climate,* **17,** 1517–1528.

Brown, R. G., and C. Zhang, 1997: Variability of midtropospheric moisture and its effect on cloud-top height distribution during TOGA COARE. *J. Atmos. Sci.,* **54,** 2760–2774.

Cau, P., J. Methven, and B. Hoskins, 2005: Representation of dry tropical layers and their origins in ERA-40 data. *J. Geophys. Res.,* **110,** D06110, doi:10.1029/2004JD004928.

Ciesielski, P. E., R. H. Johnson, P. T. Haertel, and J. Wang, 2003: Corrected TOGA COARE sounding humidity data: Impact on diagnosed properties of convection and climate over the warm pool. *J. Climate,* **16,** 2370–2384.

Comstock, J. M., T. P. Ackerman, and G. G. Mace, 2002: Ground-based lidar and radar remote sensing of tropical cirrus clouds at Nauru Island: Cloud statistics and radiative impacts. *J. Geophys. Res.,* **107,** 4714, doi:10.1029/2002JD002203.

DeMott, C. A., and S. A. Rutledge, 1998: The vertical structure of TOGA COARE convection. Part II: Modulating influences and implications for diabatic heating. *J. Atmos. Sci.,* **55,** 2748–2762.

Gallus, W. A., and R. H. Johnson, 1991: Heat and moisture budgets of an intense midlatitude squall line. *J. Atmos. Sci.,* **48,** 122–146.

Grabowski, W. W., J.-I. Yano, and M. W. Moncrieff, 2000: Cloud resolving modeling of tropical circulations driven by large-scale SST gradients. *J. Atmos. Sci.,* **57,** 2022–2039.

Hashizume, H., S.-P. Xie, W. T. Liu, and K. Takeuchi, 2001: Local and remote atmospheric response to tropical instability waves: A global view from space. *J. Geophys. Res.,* **106,** 10 173–10 185.

Hollars, S., Q. Fu, J. Comstock, and T. Ackerman, 2004: Comparison of cloud-top height retrievals from ground-based 35 GHz MMCR and GMS-5 satellite observations at ARM TWP Manus site. *Atmos. Res.,* **72,** 169–186.

Johnson, R. H., P. E. Ciesielski, and K. A. Hart, 1996: Tropical inversions near the 0°C level. *J. Atmos. Sci.,* **53,** 1838–1855.

——, T. Rickenbach, S. A. Rutledge, P. Ciesielski, and W. Schubert, 1999: Trimodal characteristics of tropical convection. *J. Climate,* **12,** 2397–2418.

Kalnay, E., and Coauthors, 1996: The NCEP/NCAR 40-Year Reanalysis Project. *Bull. Amer. Meteor. Soc.,* **77,** 437–471.

Lhermitte, R., 1990: Attenuation and scattering of millimeter wavelength radiation by clouds and precipitation. *J. Atmos. Oceanic Technol.,* **7,** 464–479.

Madden, R. A., and E. J. Zipser, 1970: Multi-layered structure of the winds over the equatorial Pacific during the Line Islands experiment. *J. Atmos. Sci.,* **27,** 336–342.

Mapes, B. E., 1997: Mutual adjustment of mass flux and stratification profiles. *The Physics and Parameterization of Moist Convection,* R. K. Smith, D. J. Raymond, and M. Miller, Eds., Kluwer Academic, Dordrecht, 399–412.

——, 2001: Water's two height scales: The moist adiabat and the radiative troposphere. *Quart. J. Roy. Meteor. Soc.,* **127,** 2353–2366.

——, and R. A. Houze Jr., 1995: Diabatic divergence profiles in western Pacific mesoscale convective systems. *J. Atmos. Sci.,* **52,** 1807–1828.

——, and P. Zuidema, 1996: Radiative–dynamical consequences of dry tongues in the tropical troposphere. *J. Atmos. Sci.,* **53,** 620–638.

——, and J. Lin, 2005: Doppler radar observations of mesoscale wind divergence in regions of tropical convection. *Mon. Wea. Rev.,* **133,** 1808–1824.

Matrosov, S., 2005: Attenuation-based estimates of rainfall rates aloft with vertically pointing K_a-band radars. *J. Atmos. Oceanic Technol.,* **22,** 43–54.

——, M. Shupe, A. J. Heymsfield, and P. Zuidema, 2003: Ice cloud optical thickness and extinction estimates from radar measurements. *J. Appl. Meteor.,* **42,** 1584–1597.

McGauley, M., C. Zhang, and N. A. Bond, 2004: Large-scale characteristics of the atmospheric boundary layer in the eastern Pacific cold tongue–ITCZ region. *J. Climate,* **17,** 3907–3920.

Moran, K. P., B. E. Martner, M. J. Post, R. Kropfli, D. C. Welsh, and K. B. Widener, 1998: An unattended cloud-profiling radar for use in climate research. *Bull. Amer. Meteor. Soc.,* **79,** 443–455.

Numaguti, A., R. Oki, K. Nakamura, K. Tsuboki, N. Misawa, T. Asai, and Y.-M. Kodama, 1995: 4–5-day-period variations and low-level dry air observed in the equatorial western Pacific during the TOGA-COAREIOP. *J. Meteor. Soc. Japan,* **73,** 267–290.

Peixoto, J. P., and A. H. Oort, 1992: *Physics of Climate.* Springer-Verlag, 520 pp.

Petersen, W. A., R. Cifelli, D. J. Boccippio, S. A. Rutledge, and C. Fairall, 2003: Convection and easterly wave structures observed in the eastern Pacific warm pool during EPIC-2001. *J. Atmos. Sci.,* **60,** 1754–1773.

Raymond, D. J., and A. M. Blyth, 1992: Extension of the stochastic mixing model to cumulonimbus clouds. *J. Atmos. Sci.,* **49,** 1968–1983.

——, G. B. Raga, C. S. Bretherton, J. Molinari, C. Lopez-Carrillo, and Z. Fuchs, 2003: Convective forcing in the intertropical convergence zone of the eastern Pacific. *J. Atmos. Sci.,* **60,** 2064–2082.

——, and Coauthors, 2004: EPIC2001 and the coupled ocean–atmosphere system of the tropical east Pacific. *Bull. Amer. Meteor. Soc.,* **85,** 1341–1354.

Redelsperger, J.-L., D. Parsons, and F. Guichard, 2002: Recovery processes and factors limiting cloud-top height following the arrival of a dry intrusion observed during TOGA COARE. *J. Atmos. Sci.,* **59,** 2438–2457.

Riehl, H., 1954: *Tropical Meteorology.* McGraw-Hill, 392 pp.

Schluessel, P., and W. Emery, 1990: Atmospheric water vapour

over oceans from SSM/I measurements. *Int. J. Remote Sens.,* **11,** 753–766.

Smull, B. F., and R. A. Houze Jr., 1987: Rear inflow in squall lines with trailing stratiform precipitation. *Mon. Wea. Rev.,* **115,** 2869–2889.

Stensrud, D. J., R. A. Maddox, and C. L. Ziegler, 1991: A sublimation-initiated mesoscale downdraft and its relation to the wind field below a precipitating anvil cloud. *Mon. Wea. Rev.,* **119,** 2124–2139.

Waugh, D., and L. Polvani, 2000: Climatology of intrusions into the tropical upper troposphere. *Geophys. Res. Lett.,* **27,** 3857–3860.

Webster, P. J., and R. Lukas, 1992: TOGA COARE: The Coupled Ocean–Atmosphere Response Experiment. *Bull. Amer. Meteor. Soc.,* **73,** 1377–1416.

Wei, D., A. M. Blyth, and D. J. Raymond, 1998: Buoyancy of convective clouds in TOGA COARE. *J. Atmos. Sci.,* **55,** 3381–3391.

Wentz, F. J., C. Gentemann, D. Smith, and D. Chelton, 2000: Satellite measurements of sea surface temperature through clouds. *Science,* **288,** 847–850.

Wijesekera, H., D. Rudnick, C. Paulson, S. Pierce, W. S. Pegau, J. Mickett, and M. Gregg, 2005: Upper ocean heat and freshwater budgets in the eastern Pacific warm pool. *J. Geophys. Res.,* **110,** C08004, doi:10.1029/2004JC002511.

Xie, P., and P. A. Arkin, 1996: Analyses of global monthly precipitation using gauge observations, satellite estimates, and numerical model predictions. *J. Climate,* **9,** 840–888.

Xie, S.-P., H. Xu, W. S. Kessler, and M. Nonaka, 2005: Air–sea interaction over the eastern Pacific warm pool: Gap winds, thermocline dome, and atmospheric convection. *J. Climate,* **18,** 5–20.

Yasunaga, K., H. Kida, and T. Satomura, 2003: The 600–750 hPa relative humidity minimum observed during PEM-Tropics B. *Geophys. Res. Lett.,* **30,** 2282, doi:10.1029/2003GL018739.

Yoneyama, K., 2003: Moisture variability over the tropical western pacific ocean. *J. Meteor. Soc. Japan,* **81,** 317–337.

——, and D. Parsons, 1999: A proposed mechanism for the intrusion of dry air into the tropical western Pacific region. *J. Atmos. Sci.,* **56,** 1524–1546.

Yuter, S. E., and R. A. Houze Jr., 1995: Three-dimensional kinematic and microphysical evolution of Florida cumulonimbus. Part II: Frequency distributions of vertical velocity, reflectivity, and differential reflectivity. *Mon. Wea. Rev.,* **123,** 1941–1963.

Zhang, C., M. McGauley, and N. Bond, 2004: Shallow meridional circulation in the tropical eastern Pacific. *J. Climate,* **17,** 133–139.

Zuidema, P., 1998: The 600–800-mb minimum in tropical cloudiness observed during TOGA COARE. *J. Atmos. Sci.,* **55,** 2220–2228.